Electromagnetic materials suited for electrified transport

Sigrid Jacobs, Jan Rens
ArcelorMittal Global R&D

Summary

Transport is responsible for about 25% of GHG emissions (IEA pre-covid-19 data). The electrification of transport has been strongly accelerated over the last 10 years, with the transition into series production of electric vehicles. After the first wave of electric bicycles, steps, scooters, carts, cars, vans, buses, came the next wave with drones, solar planes, ferries, energy harvesting ships. ArcelorMittal has followed the needs in electrical equipment from the first renewable electricity generation systems, to the highest power density machines used in electrified transport today. We have committed to becoming a carbon neutral steel manufacturer by 2050. Which is why we firmly believe that steel, as a ferromagnetic material, is the answer for the needs of the transport systems of the future. The clean energy transition is being made coherent with worldwide covid-19 recovery measures, in an integration of sustainable, resilient, interconnected and cost-effective new solutions, based on high-tech and digitalization. The move to green cargo transport is not straightforward on land, sea or air. Battery capabilities limit the deployment of large electric planes or container vessels. Any of the future systems will need electromagnetic systems for propulsion and braking with energy recuperation. Furthermore electromagnetic assistance in transport systems move beyond the replacement of hydraulic and mechanical systems, but bring also a noise and wear reduction as comfort feature. The machines designed now for transport, come in rotational or linear types. They imply a holistic approach of the machine design, its power supply, thermal management, as an integrated system.
Their ferromagnetic materials benefit from zones with very high permeability and others with very low permeability. Mechanical properties need to be tuned for manufacturing and exploitation. Thermal balances need to apply new cooling topologies, with optimal thermal conductivity materials, even in high resistivity conditions or when insulation is required. We have picked-up this material challenge and present some simulation examples, linked to material properties.
The applications shown in this paper are propulsion, braking and guidance systems. This paper

is dedicated to linear solutions, such as those for train transport, magnetic levitation systems, Hyperloop. These linear systems have a particular modelling approach and specific material requirements that will be explained further.

1. Linear brake

Electromagnetic braking is the preferred braking method to avoid mechanical friction systems, which have the disadvantage of creating noise and wear on the contact zones. Improving the performance of electromagnetic brakes is coherent with the decongestion plans of road traffic, in allowing more nightly freight transport. Obviously reduced wear, and its impact on maintenance, also is beneficial for rail system occupancy. The example modelled with JMAG starts from an existing high speed rail brake [1] and studies the impact of the selected material on the bogie and rail side. It includes the impact of eddy currents in the rail surface, in a multilayer modelling approach.

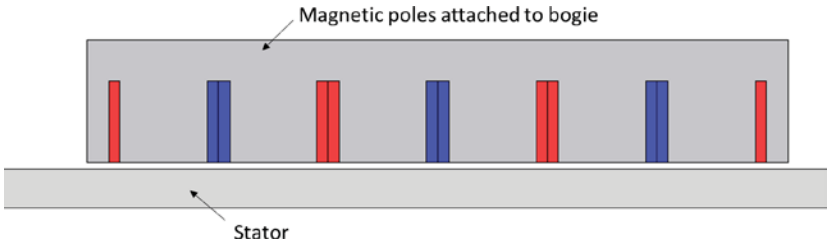

Figure 1. Layout of brake

The layout of the brake is shown in Fig. 1. It consists of a 6-pole electromagnet that is attached to the bogie, such that an airgap of 9mm is maintained above the ferromagnetic rail, which acts as the stator. A DC excitation is applied to the electromagnet, resulting in the induction of magnetic flux in the stator and, hence, eddy currents due to the relative movement between bogie and stator. More details of the brake are provided in Table 1.

Length electromagnet	1190 mm
Height electromagnet	210 mm
Depth electromagnet	135 mm
Air gap length	9 mm
Magnetic excitation	33.5 Aturns
Lamination material DC poles	0.65mm electrical steel

Table 1. Brake configuration

In the present analysis, three stator materials are compared in terms of the performance of the brake. The electrical resistivity of these materials was measured according to the 4-point resistance measurement method [IEC 60404-13], whilst the magnetic permeability was measured up to 80kA/m according to the permeameter method [IEC 60404-4]. This is realized thanks to a high number of turns on the primary side, in combination with a high power amplifier. The achieved measurement points lie well beyond the kneepoint of the magnetization graphs, implying a correct approach to saturation, as input for the modelling. The selected steel types present each a different combination of permeability and resistivity, achieved through different metallurgies. A summary of the materials is given in Table 2.

Material	DC μr at 1.5T	Resistivity (μOhm.cm)
Steel 1	455	17
Steel 2	44	30
Steel 3	60	41

Table 2. Steel types used in the stator

11 Homogeneous material approach

In a first analysis, it is assumed that the stator is composed of a homogeneous material. 2D FE simulations are carried out to study the effect of the stator material on the developed forces. Fig. 2 shows the predicted braking force as a function of the linear velocity of the train, where it can be seen that the peak force occurs at relatively small speeds, and that the material with the highest resistivity delivers the highest braking force.

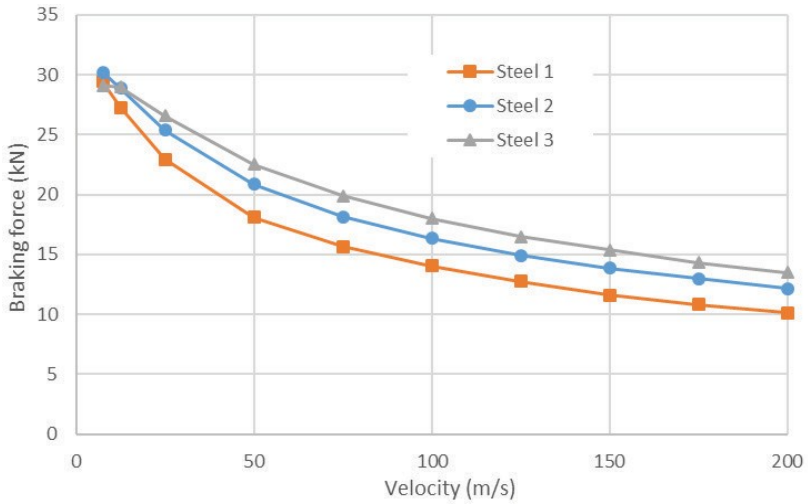

Figure 2. Braking force as a function of train velocity, for 3 stator materials

Fig. 3 shows the normal force between mover and stator as a function of velocity, which varies from an attractive force at low speeds to a repulsive force at high speeds. As in Linear Induction Machines, the attractive force originates from the interaction between the mmf of the mover and the ferromagnetic stator, whereas the repulsive force is due to the interaction between the mmf's from stator and mover [8].

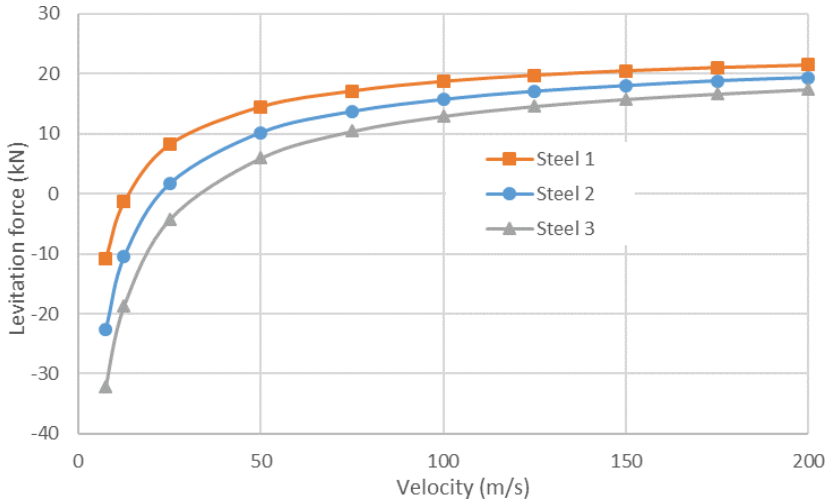

Figure 3. Levitation force as a function of train velocity, for 3 stator materials

12 Gradient material approach for the stator

In a second analysis, material properties were varied as a function of the distance from the surface of the stator, in order to demonstrate the effect of specific surface properties or the use of multi-layered materials. In the model, the stator material was implemented in layers

of 0.5mm from the surface up to a depth of 2mm. Steel 1 was used as bulk material, Steel 3 in the outer skin layer, and the intermediate layers were made from a material that is a gradual linear combination of both Steel 1 and Steel 3. The horizontal and normal forces of this configuration are shown in Fig. 4 and compared with the previous results. It appears that the use of the multi-layered material in this case results in similar forces as the low-resistivity material Steel 1.

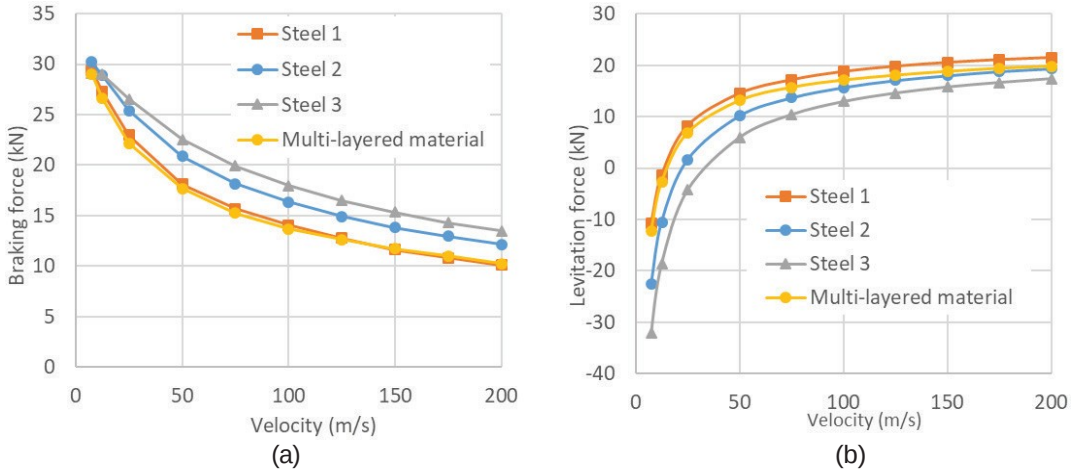

Figure 4. Braking force (a) and normal force (b) as a function of train velocity, for 4 stator materials

Figs. 5 a, b and c show those regions at the top of the stator where the current density reaches a peak value, respectively for Steel 1, Steel 3 and the multilayered material, for a linear velocity of 200m/s. It can be seen that the multi-layered material results in a peak current density occurring within the material, thus effectively increasing the skin depth. Figs 5 d, e and f similarly show the regions with peak flux density in the stator, respectively for Steel 1, Steel 3 and the multilayered material. It is again clear that the skin depth is increased compared to the stator with Steel 1. The multi-layered technique therefore can be used to optimize the stator material configuration.

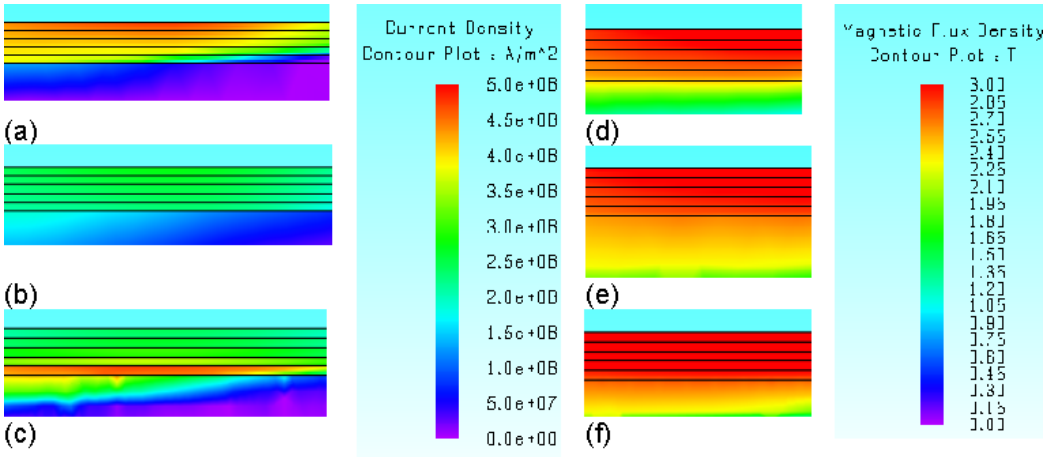

Figure 5. Current density and flux density in top layers of stator, when the brake is operating at 200m/s, and when the stator is made from respectively Steel 1 (a, d), Steel 3 (b, e) or a multilayered Material (c, f)

13 Thermal effect

In order to verify that the stator is not overheating, a 2D thermal model was generated, based on the dissipated losses from the previous transient analysis whilst ignoring convection losses. Fig. 6 shows the temperature rise in the stator when made from Steel 2, after 9 mover units

have passed at a constant velocity of 140m/s. It can be seen that the temperature rise in the top of the stator remains low at approximately 2°C each time a braking unit passes the rail.

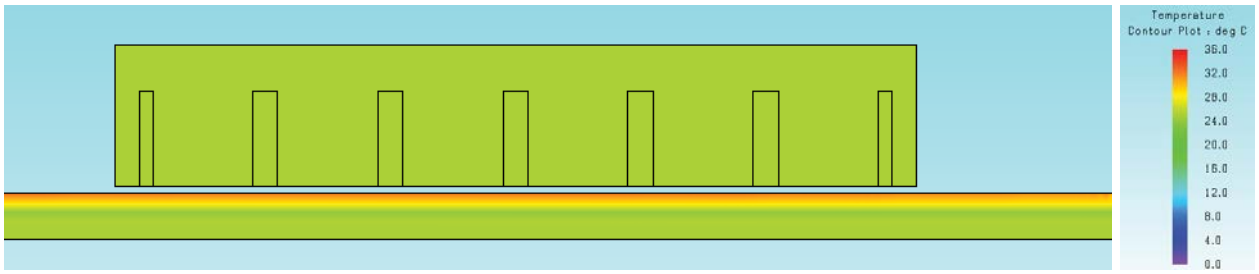

Figure 6. Temperature distribution in stator at 140m/s after 9 mover units have passed

2. Linear synchronous machine for transportation

Linear synchronous machines (LSM's) with long stators are an attractive technology for the propulsion of high-speed transportation, due to their high efficiency and high-speed capability. LSM's have been installed in the Transrapid Maglev system, which uses a conventional stator, as well as the Japanese SCMaglev, which uses superconducting coils. In this section, it is investigated how a LSM with a conventional stator performs as propulsion of a Hyperloop vehicle, for which considerably higher speed and forces are required. In a first instance, a LSM that is based on the Transrapid solution is presented. Then, the machine will be adapted to make it suitable for operation as a Hyperloop propulsion motor, taking into account space limitations that exist in Hyperloop applications. Further, the mechanical structure that is required to support the LSM is discussed. Finally, loss mechanisms in the supporting structure and the magnetic core of the machine are presented.

21 Synchronous motor for Maglev

As a starting point for the analysis, a LSM is modelled that is based on the Transrapid solution, for which some specifications are given in Table 2 [4]. This system consists of a number of magnetic units, shown in Fig. 7 [3], each consisting of a moving electromagnet that is attached to the bogie. The long active stator is equipped with a three-phase winding, which is controlled to provide both propulsion and levitation of the vehicle. For the numeric model, the LSM was simplified by ignoring the discrete distribution of magnetic units and assuming a single continuous electromagnet on the mover, thus allowing for a short, periodic 2D model. Fig. 8 shows the model and the resulting flux distribution at full load, with Table 3 providing key parameters of the model which were derived from literature [references are given in the table]. Both mover and stator are made from the electrical steel previously listed in Table 1. With the loadings given in Table 3, a total propulsion force of 104kN is predicted by the model, i.e. 22% in excess of the required 85kN (cf. Table 2). This overhead is acceptable given that the model neglects all end-effects, and it is applied to other predicted forces in this document. As can be seen in Fig. 8, the flux density in the yoke remains quite low with a maximum at around1.3T, such that it will be possible to raise the force density of the machine by increasing its loading. Finally, it must be noted that the operation below 215Hz avoids the appearance of skin effects in the laminations.

Required propulsion force	85 kN
Max speed	400 km/h
Length vehicle	54.2 m
Mass vehicle (for 400km/hr)	108 t

Table 3. Specifications of Transrapid

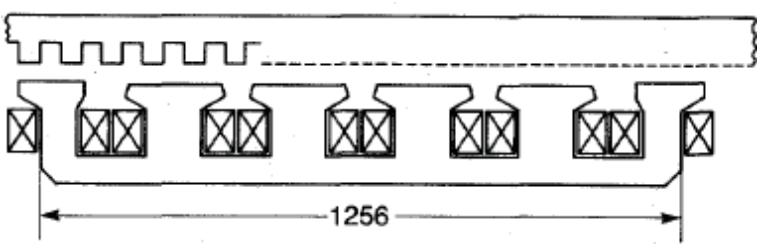

Figure 7. A “magnetic unit” in Transrapid

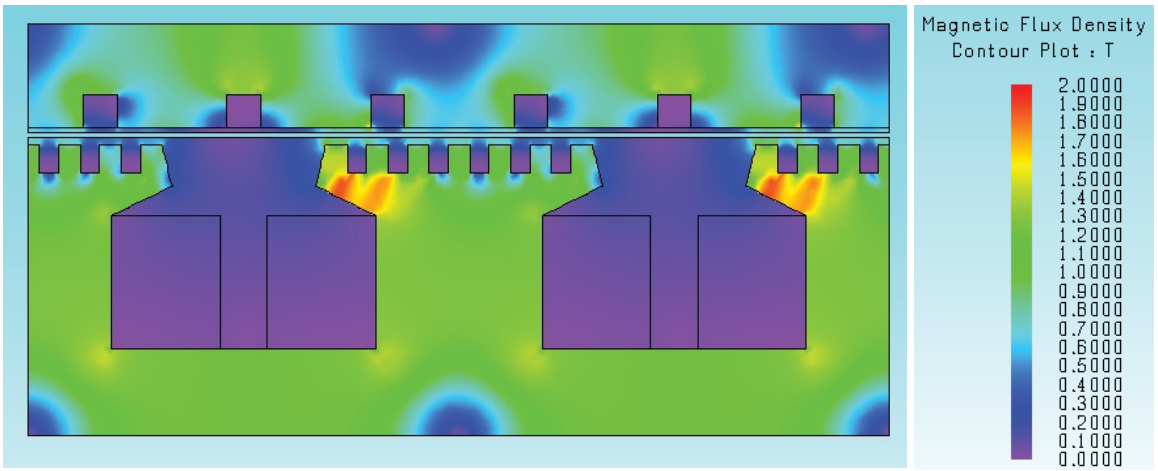

Figure 8. 2D model of the LSM, showing flux distribution at full load

Pole pitch	0.516m [3, 4, 5]
Length of LSM	40m [3]
Depth of LSM	0.185m [6]
Airgap length	10mm [4, 5, 6]
Mover mmf	5500Aturns [5]
Stator mmf	1200Aturns [4]
frequency at 400km/h	215Hz

Table 4. Parameters of LSM

22 Synchronous motor for Hyperloop

Table 5 lists typical specifications of a Hyperloop vehicle [7], demonstrating that it is a smaller and lighter vehicle compared to a Maglev, but also that it requires higher forces and operates at higher speeds.

Pole pitch	0.516m [3, 4, 5]
Length of LSM	40m [3]
Depth of LSM	0.185m [6]
Airgap length	10mm [4, 5, 6]

Table 5. Specifications of Hyperloop [7]

In the analysis, it is assumed that stringent space and weight restrictions exist in the Hyperloop tube, such that the height and depth of the stator stack of the previously studied LSM cannot be increased. Therefore, in order to meet the propulsion specifications, the mmf’s in stator and mover are equally increased until the desired force is reached. In order to avoid overheating of

the stator coils, the current density is limited to 4A/mm2 by increasing the slot area [8]. Fig. 9 shows the resulting flux density in the model at full load, where it can be seen that relatively high flux densities are reached in the stator. Some parameters of the LSM which are changed from the initial design are given in Table 5.
Due to the high magnetic fields in the machine, an attraction force of 1.4MN exists between stator and mover in the current design, which is far in excess of the required levitation force. It would therefore be impractical to use the LSM for levitation purposes, as this would require excessive control efforts. It is envisaged that the LSM is configured with two airgaps in the horizontal plane such that attraction forces are cancelled out , either as a doubly-sided machine in the center of the vehicle [7] or kept as a single-sided machine on each side of the vehicle as in the SCMaglev.
Due to the increase in operating frequency to 538Hz, attention must be paid to skin effects in the laminations, especially because a relatively high lamination thickness is considered.

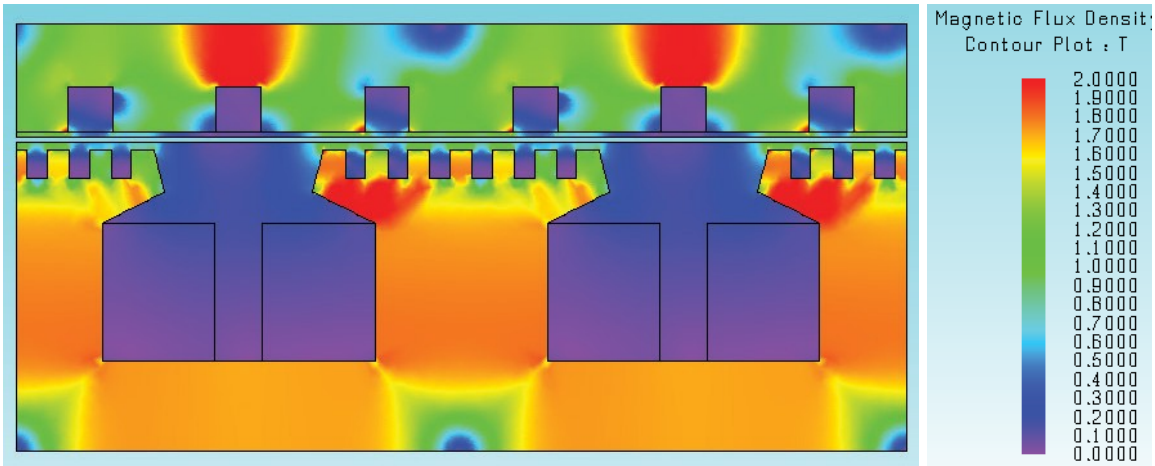

Figure 9. Flux density distribution at maximum load in LSM for Hyperloop specifications

Active length	20m
Mover mmf	9750Aturns
Stator mmf	2150Aturns
Frequency at 1000km/h	538Hz

Table 6. Parameters of LSM for Hyperloop specification [7]

23 Supporting structure

During operation, considerable mechanical loads are exerted on the stator, caused by strong oscillations in propulsion and attraction forces. Such oscillations arise from the large slot openings in mover and stator, and also from the discontinuous configuration of the mover by using discrete magnetic units (cf. Fig. 7) which result in the stator being locally subjected to a rapid rise in loads when a unit passes.
The design of a rigid support structure, which attaches the laminated stator to the guideway, is thus essential. However, because support structures generally consist of solid metallic parts, they are prone to high magnetic losses due to the presence of magnetic stray fields, which are exacerbated by the high flux operation of the machine.
To support the LSM previously presented, a comparison is made between two configurations, being the use of dovetailed connectors and the use of rigid plates or housing. Further, for each configuration, the support material is compared between Steel 1 (cf. Table 1) and austenitic stainless steel.

2.3.1 Use of dovetail connectors

Fig. 10 shows a supporting structure for a Transrapid vehicle, which uses dovetail connectors that are themselves screwed into an overhanging support structure at some distance above the stator [9]. When this solution is applied to Hyperloop, the number of connectors needs to be increased, due to the generation of a force density which is around three times higher in comparison to typical loads seen in the Transrapid. A transient magnetic 2D model was built to estimate the effect on losses and force generation. It was assumed that the connectors were electrically insulated from the overhanging structure to avoid large circulating currents. As can be seen in Fig. 11 which shows the flux density at full load with the structure made from Steel 1, the apertures in the yoke that are necessary to insert the connectors increase the flux-density in the yoke, resulting in significant flux leakage through the structure.

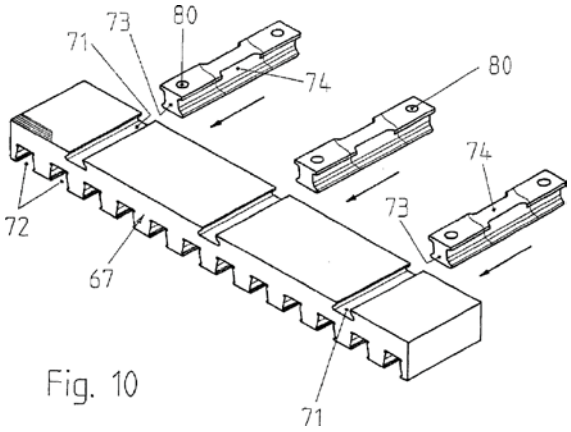

Figure 10. Dovetailed connectors, proposed for support of Transrapid solution [8]

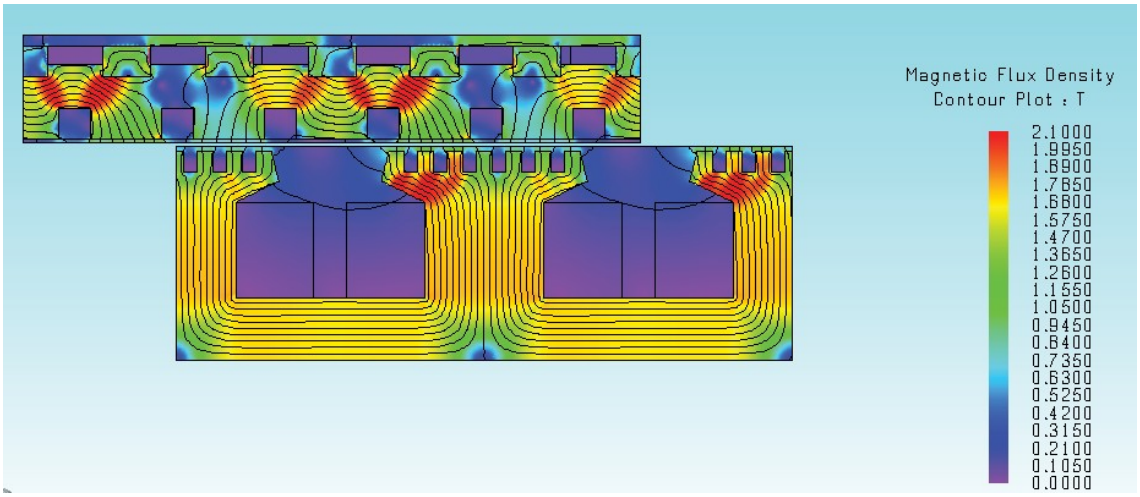

Figure 11. Flux density prediction in LSM when supported using dovetail connectors, at full load conditions and with the structure made from Steel 1

2.3.2 Use of support plate

An alternative to the dovetailed connectors consist of providing a plate support at the backside of the stator, which is sufficiently rigid to support the loads and can be directly connected to the guideway.. In this case, the support is continuously connected with the yoke. Also, the stator laminations are not affected, resulting in a lower flux density in and lower flux leakage through structural parts, as shown in Fig. 12.

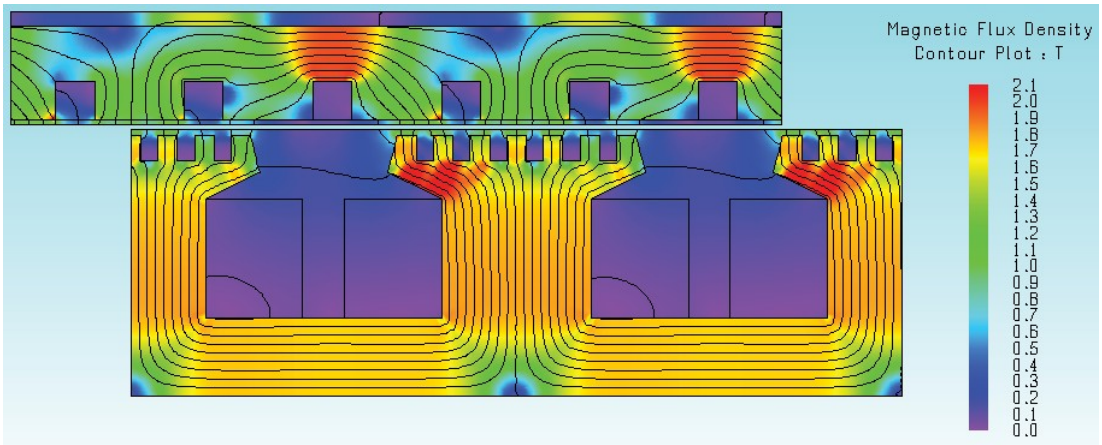

Figure 12. Flux density in LSM with a supporting plate made from Steel 1

2.3.3 Comparison

Table 7 lists the magnetic losses in the supporting structure of the LSM when the Hyperloop is operating at 1000km/h, for two materials and two support configurations. Firstly, it can be seen that the use of austenitic stainless steel results in considerably lower losses, as expected, due to its low permeability and high electrical resistivity. Also, it can be noted that the dovetailed solution results in high losses, as a consequence of the high stray magnetic fields that are caused by the apertures in the yoke. The fact that the support above the dovetail connectors has an airgap with the stator, does not bring an advantage in terms of losses, in this configuration. The effect of the support structure on the propulsion force is shown in Fig. 13, where it can be concluded that, for the current design, the use of dovetailed connectors has some negative impact on the force generation. In case of stainless steel connectors, this reduction is due to the paramagnetic nature of the material, resulting in an increased reluctance of the yoke caused by the apertures. In case of the Steel 1 connectors, the force reduction is due to the drag force generated by the high losses.

Dovetail Support plate	Steel 1 1786kW 207kW	Austenitic stainless 361kW 48kW

Table 7. Comparison of losses in support structure at 1000km/h

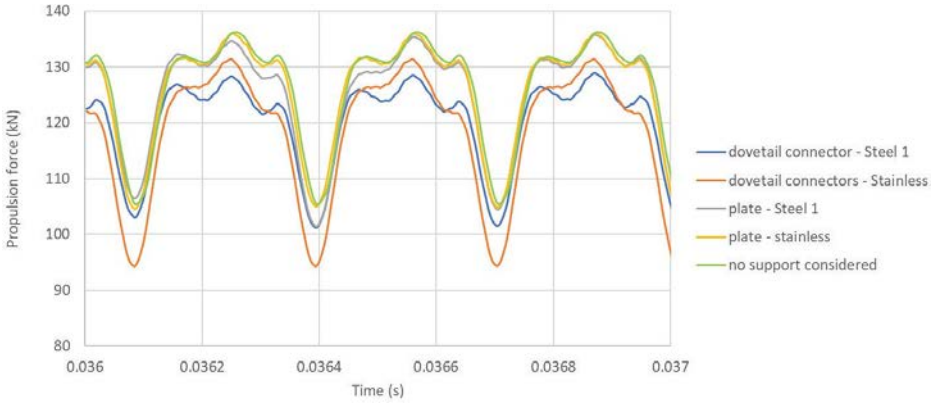

Figure 13. Propulsion force for different support configurations

2.4 Core losses in stator laminations

Two methodologies are compared to calculate the core losses in the stator laminations. Firstly, the statistical loss theory that is based on the separation of losses into hysteresis, excess and classical loss components is used. Secondly, post-processing methods that are implemented in JMAG to account for eddy-current loss and hysteresis loss are used.

2.4.1 Statistical loss modelling

A general and wide-spread approach to core loss modelling is based on the separation of losses into hysteresis, excess and classical loss components. According to the statistical loss theory, the loss components can be described as a function of frequency and polarization, and can thus be expressed as shown in eq. 1 [10].

$$P = P_{hyst} + P_{exc} + P_{class} = k_{hyst}(J)f + k_{exc}(J)f^{1.5} + k_{class}(J)f^2 \quad (1)$$

The loss model relies on the availability of measurement data covering a large number of frequencies and polarization levels, allowing to derive material-specific core loss parameters by fitting eq. (1) to the data.

Using this model, the losses in the LSM are calculated in a post-processing configuration. First, the FE model is simulated for a single electrical period using a large number of timesteps. Then, using a post-processing script, the waveforms of magnetic field and polarization are constructed in each mesh element by collecting the solutions at different timesteps. This allows for the different loss components to be calculated in each element of the mesh, and thus in the overall machine.

2.4.2 JMAG toolboxes for loss calculation

JMAG has implemented a number of methods to calculate hysteresis and dynamic losses, either de-coupled in a post-processing mode or coupled whilst solving the main field calculations. For each loss component, one method was selected to compare with the statistical loss methodology.

For the calculation of dynamic losses, the 2D1D methodology was used in a post-processing condition. This method solves, for each node of the mesh, a 1D eddy-current model in the direction of the thickness of the lamination, in combination with the 2D model in the plane of the lamination where homogeneous material properties are assumed. The 2D1D calculation methodology was compared with the modelling of a single lamination in 3D under the same conditions, resulting in very similar eddy current loss prediction. The 3D model calculates the eddy current distribution during the main field calculation, and further improves on the 2D1D method by including end effects in the edges of the lamination. Fig 14 (a) shows the 3D model, whilst Fig 14 (b) shows the flux density through a cut of a stator tooth, clearly demonstrating the magnetic skin effect throughout the thickness of the lamination. For the hysteresis losses, the Hysteresis Model is used in the post-processing mode. The measured hysteresis curves are converted through a Play Model approach to a mathematical description of the Preisach distribution. The Preisach approach of hysteresis consists of describing a generic hysteretic system as the superposition of many bi-stable units, which interprets magnetization as a series of Barkhausen instabilities [11]. The Play and Stop model represent hysteretic characteristics equivalent to the scalar static Preisach model [12]. The play model + 1D eddy current approach is documented by JMAG [13]. This material description is combined with the magnetic flux density history that is the result of the FE simulation, to obtain the losses.

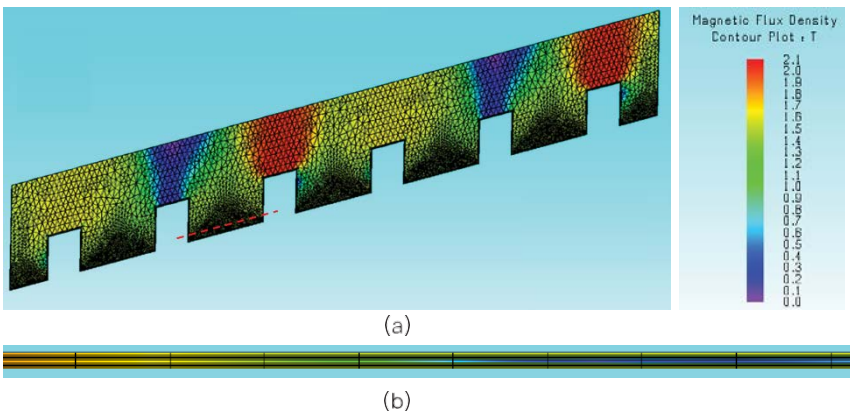

Figure 14. (a) Flux density in 3D model of a single stator lamination; (b) Flux density on a cut through a stator tooth. The position of the cut is shown on Fig14 (a)

2.4.3 Comparison of losses

Table 8 compares the loss predictions from both methods previously described. It can be seen that both loss predictions give similar results, although the calculation methodology differs considerably. Further, the predicted stator core losses are significant and represent around 10% of the power capability of the Hyperloop. This is due to the high magnetic fields and frequency at which the LSM operates, and the material choice for the stator laminations which is not suited for the demanding Hyperloop specifications.

	JMAG 2D1D	JMAG 3D	Statistical loss model
Quasi-static losses (hysteresis)	283 kW	223 kW	319 kW
Dynamic losses (classical+excess)	2931 kW	2799 kW	2701 kW
Sum	3214 kW	3022 kW	3020 kW

Table 8. Comparison of predicted losses in stator laminations. All values are expressed in kW and are given for the entire LSM at full load and 1000km/h

The hysteresis losses are lower in the 3D calcs. This is due to the expected lower flux density in this fully coupled model. The flux redistribution is best taken into account in the 3D model.

3. Conclusions

This paper covers, within electrified transport, specifically the linear machine requirements, for high speed transport such as Rail and Hyperloop. The analyzed active materials are either laminated or bulk steel types. The focus lies on the achievable combinations of permeability/saturation and resistivity, and their impact on the machine performance in terms of force development, flux redistribution and losses, in particular in these applications ruled by the presence of high frequency fields. The approach is based on advanced material characterization techniques, including (1) high field magnetization measurements to correctly include the approach to saturation in the models, (2) identification of the Preisach distribution function based on multiple hysteresis measurements and JMAG's Play / Stop models, (3) eddy current analysis including skin effect, (4) gradient material measurements of thin layer samples. The results show the importance of proper selection of not only the active materials in the machine, but also the importance of structural parts of the machines in their assembly structure. Specific steel developments provide dedicated solutions. Such linear machines, for high speed applications, have particular material issues linked to skin effect, and modelling issues linked to boundary conditions and complex topologies that easily become too difficult to master. ArcelorMittal welcomes the challenge these developments bring.

4. References

[1] M. Homann, Th. Werle, R. Pfeiffer and A. Binder, '2D and 3D Numerical Field Computation of Eddy-Current Brakes for Traction", IEEE Transactions on Magnetics, Vol. 36,No. 4, July 2000
[2] Ion Boldea, "Linear Electric Machines, Drives and MAGLEVs Handbook", CRC Press, 2013
[3]G. Bohn and G. Steinmetz, "The Electromagnetic Levitation and Guitande Technology of the 'Transrapid' Test Facility Emsland", IEEE Transactions on Magnetics, Vol. 20, No 5, September 1985
[4] J. Meins, L. Miller and W. J. Mayer, "The High Speed Maglev Transportation System Transrapid", IEEE Transactions on Magnetics, Vol. 24, No. 2, March 1988
[5] M. Andriollo, G. Martinelli, A. Morini and A. Tortella, "FEM Calculation of the LSM Propulsion Force in EMS-MAGLEV Trains", IEEE Transactions on Magnetics, Vol. 32, No. 5, September 1996
[6] A. Cassat, M. Jufer, "MAGLEV Projects, Technology Aspects and Choices", IEEE Transactions on Applied Superconductivity, Vol. 12, Issue 1, March 2002

[7] W.-Y. Ji, G. Jeong, Ch.-B. Park, I.-H. Jo and H.-W. Lee, "A Study of Non-Symmetric Double-Sided Linear Induction Motor for Hyperloop All-In-One System (Propulsion, Levitation, and Guidance)", IEEE Transactions on Magnetics, Vol. 54, No. 11, November 2018
[8] US Patent, "Process for Producing an Electromagnetic Subassembly for a Magnetic Levitation Railway", US 6.584.671 B2, July 2003
[9] US Patent, "Structure for Supporting Trackway of a Track following Transportation System, in Particular, a Magnetic Suspension Railroad, US005370.059A", Dec 1994
[10] G. Bertotti, "Physical interpretation of eddy current losses in ferromagnetic materials", J. Appl. Phys 1985, 57, 2110–2117
[11] G. Bertotti, "Hysteresis in magnetism", Academic Press, ISBN: 0-12-093270-9, 1998
[12] T. Matsuo, D. Shimode, Y. Terada, M. Shimasaki, "Application of Stop and Play Models to the Representation of Magnetic Characteristics of Silicon Steel Sheet", IEEE Transactions on Magnetics, Vol. 39, No. 3, May 2003
[13] JMAG, "Understanding Electromagnetic Phenomena in Steel Sheets Through Simulation", W-MA-51, May 2018